Title

Evolution of Multivalent Nanoparticle Adhesion via Specific Molecular Interactions

Journal

Langmuir, 32(49)

ISSN

0743-7463

Authors

Wang, Mingqiu

Ravindranath, Shreyas R

Rahim, Maha K

et al.

Publication Date

2016-12-13

DOI

10.1021/acs.langmuir.6b03014

HHS Public Access

Author manuscript

Langmuir. Author manuscript; available in PMC 2017 December 13.

Published in final edited form as:

Langmuir. 2016 December 13; 32(49): 13124–13136. doi:10.1021/acs.langmuir.6b03014.

Evolution of Multivalent Nanoparticle Adhesion via Specific Molecular Interactions

Mingqiu Wang[†], **Shreyas R. Ravindranath**[†], **Maha K. Rahim**[†], **Elliot L Botvinick**[†,‡,∥,⊥,#], and **Jered B. Haun**[*,†,§,∥]

[†]Department of Biomedical Engineering, University of California—Irvine, Irvine, California 92697, United States

[‡]Department of Surgery, School of Medicine, University of California—Irvine, Irvine, California 92697, United States

[§]Department of Chemical Engineering and Materials Science, University of California—Irvine, Irvine, California 92697, United States

[∥]Chao Family Comprehensive Cancer Center, University of California—Irvine, Irvine, California 92697, United States

[⊥]Beckman Laser Institute, University of California—Irvine, Irvine, California 92697, United States

[#]Edwards Lifesciences Center for Advanced Cardiovascular Technology, University of California—Irvine, Irvine, California 92697, United States

Abstract

The targeted delivery of nanoparticle carriers holds tremendous potential to transform the detection and treatment of diseases. A major attribute of nanoparticles is the ability to form multiple bonds with target cells, which greatly improves the adhesion strength. However, the multivalent binding of nanoparticles is still poorly understood, particularly from a dynamic perspective. In previous experimental work, we studied the kinetics of nanoparticle adhesion and found that the rate of detachment decreased over time. Here, we have applied the adhesive dynamics simulation framework to investigate binding dynamics between an antibody-conjugated, 200-nm-diameter sphere and an ICAM-1-coated surface on the scale of individual bonds. We found that nano adhesive dynamics (NAD) simulations could replicate the time-varying nanoparticle detachment behavior that we observed in experiments. As expected, this behavior correlated with a steady increase in mean bond number with time, but this was attributed to bond

[*]**Corresponding Author:** Phone: 949-824-1243. jered.haun@uci.edu. Home page: http://haun.eng.uci.edu.

Supporting Information

The Supporting Information is available free of charge on the ACS Publications website at DOI: 10.1021/acs.langmuir.6b03014. Methods describing nanoparticle motion, force calculations, determination of intrinsic bond formation and breakage rates, and bond mechanical property measurements using optical tweezers. Figures for optimizing simulation parameters, total bond numbers versus time and γ, bond biophysics and reaction rates under different γ conditions, bond number dynamics, corrected bond distributions, optical-tweezers-based dynamic force spectroscopy, bond numbers for all ICAM-1 configurations, mean bond potential for dimer and monomer cases, and nanoparticle detachment dynamics in single bond simulations. Tables for nanoparticle dynamics at low and high antibody densities for different γ values. Simulation results for all valency conditions at $\sigma = 0.8$ N/m using the dimer and the monomer configurations. (PDF)

Notes

The authors declare no competing financial interest.

accumulation only during the first second that nanoparticles were bound. Longer-term increases in bond number instead were manifested from nanoparticle detachment serving as a selection mechanism to eliminate nanoparticles that had randomly been confined to lower bond valencies. Thus, time-dependent nanoparticle detachment reflects an evolution of the remaining nanoparticle population toward higher overall bond valency. We also found that NAD simulations precisely matched experiments whenever mechanical force loads on bonds were high enough to directly induce rupture. These mechanical forces were in excess of 300 pN and primarily arose from the Brownian motion of the nanoparticle, but we also identified a valency-dependent contribution from bonds pulling on each other. In summary, we have achieved excellent kinetic consistency between NAD simulations and experiments, which has revealed new insights into the dynamics and biophysics of multivalent nanoparticle adhesion. In future work, we will leverage the simulation as a design tool for optimizing targeted nanoparticle agents.

Graphical abstract

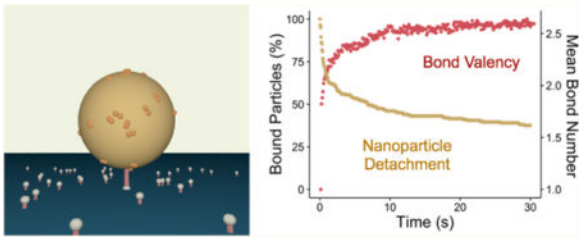

INTRODUCTION

The targeted delivery of imaging or therapeutic agents to disease sites within the body still remains a major medical goal even after decades of research. Nanoparticle carriers offer numerous advantages as a delivery platform, including high-loading capacity and protection of agents, facile attachment of affinity molecules, and favorable pharmacokinetics.[1–3] Another powerful attribute is the ability to form multiple bonds with target cells, thereby improving the overall adhesion strength and internalization rate into cells.[4–13] However, our understanding of multivalent nanoparticle adhesion has primarily been based on thermodynamic behavior. For example, binding performance has typically been assessed after systems have reached equilibrium, and results were assessed in terms of an apparent affinity, also termed the avidity. Another issue is that it is nearly impossible to control for differences in context between different experimental systems. Thus, critical knowledge gaps remain in the field regarding the time course by which nanoparticles evolve from initial capture via one or more bonds to the final multivalent state as a function of different system parameters. Such information would be extremely powerful for designing nanoparticle carriers that exhibit optimal targeting performance for different disease scenarios.

In previous work, we developed a unique framework for assessing multivalent nanoparticle adhesion from a kinetic viewpoint.[6,8,11] Specifically, we determined the rates of attachment (k_A) and detachment (k_D) for nanoparticles mediated by the interaction between an antibody and ICAM-1 in flow chamber assays. We concluded that k_D was not a constant in time but rather decreased following a power law relationship that contained magnitude $(k_D{}^0)$ and

temporal (β) parameters. Furthermore, we found that β was constant over a broad range of antibody and ICAM-1 densities and particle sizes (40 nm to 1 μm).[6,8] However, β did vary for different types of binding interactions, such as recombinant single-chain antibodies and avidin/biotin.[11] Although our kinetic approach has provided unique insights into multivalent nanoparticle adhesion, we do not yet understand the underlying mechanisms behind the time-dependent detachment rate phenomenon, most notably the number and dynamic behavior of individual bonds.

Numerous computational approaches have been developed in an effort to understand multivalent binding phenomena. The most common approach has been to partition multivalent species into discrete bond valence states that are attributed to an overall thermodynamic free energy.[14–16] In this manner, the Dormidontova group used Monte Carlo simulations to investigate the multivalent binding of polymer-coated nanoparticles under different bond density, energy, length, and clustering conditions to determine the overall effects on the binding free energy.[17–19] Martinez-Veracoechea et al. later presented a numerical simulation that calculated binding free energies using statistical mechanical functions, which led to the first prediction of superselective behavior.[20] Although the above works offer useful insights into multivalency, they included little to no discrete bond detail beyond the chemical energy, notably lacking a role for mechanical forces. It is well established that applied forces accelerate the rupture of noncovalent, biomolecular bonds by lowering the potential energy barrier.[21–26] Decuzzi et al. incorporated bond mechanical considerations by modeling bonds as Hookean springs to determine the bond force and then using the Bell model to predict the effects of force on the bond rupture rate.[27] A stochastic multivalent nanoparticle binding model was then used to predict the adhesion strength to cells and the probability of endocytosis. Liu et al. later used a Metropolis Monte Carlo simulation and a weighted histogram analysis to quantify the binding free energy of antibody-coated nanoparticles to endothelial cells via ICAM-1, which matched equilibrium adhesion data obtained from experiments.[28] Furthermore, mechanical force predictions on the order of 200 pN were corroborated using atomic force microscopy. Although these works have been illuminating, the focus remained solely on the equilibrium behavior. To date, temporal dynamics of multivalent nanoparticle adhesion has been studied only by Wang et al. using dissipative particle dynamics simulations.[29] The number of bonds and the time constant required to reach equilibrium were studied at different overall binding strengths, but bond kinetics and biophysics were not evaluated. Thus, a simulation approach combining dynamic analysis of nanoparticle adhesion with discrete bond kinetic and mechanical properties has not yet been demonstrated.

Adhesive dynamics is a simulation framework originally developed to model kinetic and biophysical aspects of leukocyte rolling adhesion to inflamed endothelium.[30] The method employs a combination of deterministic equations of motion for the cell and a probabilistic treatment for bond formation and breakage. Bonds are modeled as Hookean springs, and the Bell model is used to establish the effect of force on both bond rupture and formation rates. Within discrete time steps, all forces are vectorially summed, the cell is translated and rotated, and bond breakage and formation are assessed on the basis of chemical and mechanical considerations using a Monte Carlo algorithm. Adhesive dynamics simulations have achieved considerable success replicating rolling, weak, and firm binding behavior of

neutrophils, protein-coated microbeads, and platelets.[30–37] The general adhesive dynamics approach was also adapted to model the binding of human immunodeficiency virus (HIV) to cells. Brownian motion was introduced into the simulation due to the nanoscale size of HIV, around 100 nm, and thus the methodology was termed Brownian adhesive dynamics (BRAD).[38–40] To date, adhesive dynamics simulations have not been used to model the multivalent adhesion of targeted nanoparticles.

In this work, we develop nano adhesive dynamics (NAD) simulations to study the kinetics and biophysics of multivalent nanoparticle adhesion. We include Brownian motion and hydrodynamic fluid flow to replicate nanoparticle adhesion within a flow chamber, and simulations are initiated with the nanoparticle bound to a planar substrate via a single bond tether in order to focus on the temporal dynamics of nanoparticle detachment and multivalent bond formation. The results are compared to previous experimental work using a 210 nm polystyrene sphere coated with a monoclonal antibody and a glass substrate coated with ICAM-1, for which all model parameters are known except the bond mechanical properties (reactive compliance, γ, and spring constant, σ).[6] We show that NAD simulations display time-dependent nanoparticle detachment behavior, which recapitulates experimental results for several different mechanical property combinations. We conclude that the key requirement to match experiments is that bonds rupture under an amount of mechanical work that is equivalent to the bond chemical energy. We then perform optical tweezers force spectroscopy experiments to determine that $\gamma = 0.27$ nm and apply this result to simulations to find that $\sigma = 0.8$ N/m provides the best fit to experiments across a broad range of adhesion molecule density conditions. As expected, time-dependent nanoparticle detachment is accompanied by an increase in the mean bond number with time. However, we conclude that the bond steady state is attained within the first 1 s after binding, and thus longer-term increases the bond number are not due to bond accumulation. Instead, we find that the nanoparticle population is heterogeneous with respect to the maximum number of bonds that each nanoparticle can form and detachment is most likely for those that are restricted to low valency. Thus, detachment serves as a selection mechanism to evolve the remaining nanoparticle population toward higher valency and overall adhesion stability. Taken together, we conclude that our phenomenological detachment rate captures the two critical aspects of valency selection. The magnitude parameter k_{D}^{0} represents the combined detachment rate for the initial nanoparticle population across all valency potentials, and the temporal parameter describes the valence-state-dependent rate at which nanoparticles are lost with time. We also conclude that the average bond lifetime is extremely short, on the order of 0.1 s, because of applied mechanical forces in excess of 300 pN. Examining our simulation, we find that mechanical force primarily arises from the Brownian motion of the nanoparticle, but we also note a contribution from bonds pulling on each other that increases with valency. In summary, NAD simulations show remarkable kinetic consistency with experiments, allowing us to uncover the mechanisms underlying time-dependent nanoparticle detachment and identify a key role for mechanical forces. Future work will seek to expand the scope of NAD simulations to also model nanoparticle tethering, explore new parameter property regimes, and adapt to cellular and *in vivo* environments. These capabilities will advance the work toward predictive applications, enabling NAD simulations to serve as a powerful design tool for optimizing nanoparticle adhesive behavior in different disease contexts.

METHODS

General Description of the Model

The NAD simulation was built upon the same principles as adhesive dynamics for modeling the dynamic binding of leukocytes under shear flow and Brownian adhesive dynamics for modeling HIV docking.[30,38–40] We have included both hydrodynamic fluid flow and Brownian motion to model nanoparticle adhesion within a flow chamber. For this study, we employed a 210-nm-diameter sphere decorated with a monoclonal antibody and a planar substrate decorated with ICAM-1 protein, as in our previous experiments.[6] The NAD process flow is shown in Figure 1. The nanoparticle and substrate were first defined, followed by a random distribution of adhesion molecules at specific total densities. A single bond was then placed between the nanoparticle and substrate at its equilibrium length. This initial condition was used because our primary goal was to monitor multivalent bond formation and time-dependent nanoparticle detachment dynamics (β and k_{D}^{0} parameters), and this is similar to a previous study that used the completed double-layer boundary integral equation method (CDL-BIEM), with Brownian motion introduced as an external force, to investigate the effect of Brownian motion on platelet adhesion via GPIb-α.[41] We also found that the initial bond length did not significantly bias the results (Supporting Information, Figure S1). Simulations were then started using a defined time step (Δt). Within each time step, bonds were assessed for potential breakage, unbound adhesion molecules were examined for potential bond formation, forces were vectorially summed, and the nanoparticle was translated and rotated. We note that the tethering of a nanoparticle from the bulk could readily be studied using the methods described, in similar manner to previous BRAD simulations.[38–40]

Nanoparticle Motion

Nanoparticle motion was determined using the Langevin equation, as in previous BRAD simulations.[40] Detailed descriptions are provided in the Supporting Information. Briefly, translational and rotational trajectories resulting from random thermal motion and all deterministic forces and torques, including hydrodynamic shear, bonding, and steric repulsion between the nanoparticle and substrate, were solved numerically.[42,43] The bond force was (F_{B}) estimated by modeling bonds as Hookean springs

$$\vec{F}_{\mathrm{B}} = \sigma(\lambda - \lambda_{\mathrm{e}})\frac{\vec{r}_{\mathrm{l}} - \vec{r}_{\mathrm{r}}}{\lambda} \quad (1)$$

where σ is the spring constant, λ is the length of the bond, λ_{e} is the equilibrium length of the bond, $\mathbf{r}_{\mathrm{r}}$ is the position vector originating from where the antibody is attached to the nanoparticle surface, and $\mathbf{r}_{\mathrm{l}}$ is the position vector originating from where ICAM-1 is attached to the substrate. For convenience, we will define the term $\delta = |\lambda - \lambda_{\mathrm{e}}|$, which determines the length that the bond is stretched or compressed from its equilibrium length. Steric repulsion between the nanoparticle and substrate surfaces was determined on the basis of the compression of a surface protein layer using a nonspecific repulsion model.[44] Finally, the shear force acting on the nanoparticle was modeled using theoretical relationships from

Goldman, Cox, and Brenner that are valid near the wall region.[45] Note that because we are now using a nanoparticle, we employed the shear force/torque relationships valid for large h/R, where R is the particle radius and h is the distance of its center from the wall.

Bond Formation and Breakage

Noncovalent biomolecular bonds stochastically fluctuate between bound and unbound states on the basis of intrinsic chemical energy, which is generally described as a thermally assisted escape over a potential energy barrier. Applying an external force to the bond lowers this energy barrier, accelerating rupture.[21–26] We used the Bell model to capture the effect of force on the rate constant for bond rupture (k_r)

$$k_r = k_r^0 \, exp \, \frac{\gamma \left| \vec{F}_B \right|}{k_B T} = k_r^0 \, exp \, \frac{\gamma \sigma \delta}{k_B T} \quad (2)$$

where k_r^0 is the intrinsic reverse reaction rate constant observed in the absence of force, γ is the bond reactive compliance that characterizes the sensitivity to force, k_B is the Boltzmann constant, and T is the absolute temperature. The term $\gamma\sigma\delta$ effectively defines the amount of mechanical work applied to the bond by force. Within each time step, the cumulative probability of rupture (P_r) was calculated for each bond as follows:

$$P_r = 1 - exp(-k_r \Delta t) \quad (3)$$

A uniformly distributed random number was then generated for each bond, and if the random number was less than P_r, then the bond was considered to have broken.

Bond formation is similarly influenced by the distance separating two adhesion molecules, which can consist of two steps: first the adhesion molecules must come sufficiently close to each other, and only then can the bond form at its intrinsic rate. The first step requires extension or compression of the unbound adhesion molecules, invoking an energetic penalty on bond formation that can again be captured using a Hookean spring model.[46] The rate constant for bond formation (k_f) was thus

$$k_f = k_f^0 \, exp \, \frac{-\sigma_{ts} (x_m - \lambda_e)^2}{2 k_B T} \quad (4)$$

where k_f^0 is the intrinsic rate of bond formation and σ_{ts} is the transition-state spring constant that applies to unbound adhesion molecules. Within each time step, the cumulative probability of formation (P_f) was calculated for all possible interactions between unbound adhesion molecules as follows:

$$P_f = 1 - exp(-k_f \Delta t) \quad (5)$$

A uniformly distributed random number was generated for each potential bonding interaction. If the random number was less than P_f, then a bond was considered to have formed. To save computational cost, potential bonds included only adhesion molecule pairs that were reasonably close to each other, which we defined as having $P_f > 10^{-6}$. Truncation of the probability density function in this manner introduced an error of <0.01% into the cumulative probability of bond formation.

Physical Representation of Adhesion Molecules

Both the antibody and ICAM-1 molecules were randomly immobilized on their respective surfaces as dimers to reflect experimental conditions (Figure 1). Antibodies consist of two Fc stalks, each of which connects to flexible binding arms (Fab). ICAM-1 protein was purchased as a chimera with human IgG1 Fc, which was reported to be a dimer by the manufacturer (R&D Systems) due to disulfide bonding within the Fc domain. To represent dimers, we randomly separated the two molecules by a distance ranging from 5 to 10 nm for antibody Fab domains and 0.5–2 nm for ICAM-1/Fc. These values were chosen from published crystal structures or our best estimates. It should also be noted that ICAM-1/Fc was linked to the surface using protein G, which contains two Fc binding domains. We initially assumed that only one of those binding domains was occupied with an ICAM-1 dimer, but it is possible that both could be occupied.

To reduce computational burden, we did not track the motion of the free end of adhesion molecules about their fixed attachment points on the nanoparticle and substrate. Instead, it was assumed that all molecules were oriented normal to their binding partners when bound or potential binding partners when unbound. This is a reasonable assumption for bonds under tension, and thus the bond length was calculated on the basis of the distance separating the attachment points on the nanoparticle and substrate. For unbound molecules, the assumption effectively implies that the moelcules can fully sweep out their local area in search of a binding partner during the course of a single time step. We did implement an algorithm to prevent a new bond from forming if it would intersect with a current bond. This was determined on the basis of the minimum distance that would separate the central axes of the potential and actual bonds. If the separation distance was less than 2 nm, which was again chosen on the basis of crystal structures and our best estimate, then the new bond was not allowed to form. This check to prevent bond crossing lowered the total bond numbers by as much as 40% (Supporting Information). Once the bonds had formed, we did not assess whether they crossed each other as the nanoparticle underwent translational and rotational motion in an effort to save computational cost.

Parameters

All parameter values used in this study are given in Table 1. The macroscopic kinetic rates for the anti-ICAM-1 antibody (clone BBIG) and human ICAM-1 binding interaction were measured by surface plasmon resonance to be 1.6×10^5 M^{-1} s^{-1} for formation and 1.1×10^{-4} s^{-1} for rupture.[47] These were converted to intrinsic rate constants (k_f^0, k_r^0) for individual bonds using the method described by Bell et al. (Supporting Information).[21] Antibody and ICAM-1 densities were based on previous experiments, which reflect the total ICAM-1 binding sites (i.e., Fab domains) and ICAM-1 molecules.[6] Molecular lengths were

estimated on the basis of crystal structures, as previously presented.[11] The fluid was assumed to be water flowing with a wall shear rate of 100 s^{-1}. The steric repulsion force between the nanoparticle and substrate was determined by estimating the surface protein layer thickness on the substrate (τ = 5 nm) and then tuning the compressibility (ξ) to be the minimum value required to prevent the nanoparticle from penetrating the adhesive substrate. The time step (Δt) was 1 ns, similar to previous adhesive dynamics and BRAD simulations.[30,38–40] Δt is also very close to the viscous relaxation time (Supporting Information), so it can be assumed that the particle has no inertia. The only unknown parameters in our model were related to bond mechanics (γ, σ, σ_{ts}). To reduce our parameter investigation, we assumed that σ and σ_{ts} had similar values, which mechanistically means that the spring constant was the same for both bound and unbound states. Although this assumption is reasonable on its own merit, we have also mitigated the importance of σ_{ts} by immediately assessing for bond breakage following each formation event. Thus, all new bonds must survive at least one rupture challenge before they can exert a force and/or torque on the nanoparticle.

Determination of Nanoparticle Detachment Rate Parameters (β, k_D^0) from Simulations

To recreate nanoparticle detachment profiles from experiments, we combined the results from an ensemble of NAD simulations. As discussed above, nanoparticles were initially bound to the substrate via a single bond at its equilibrium length. Simulations were then performed until a predefined simulation time was reached or the nanoparticle translated from its initial location by a distance that was at least 2.5 times its diameter. The latter condition was designed to replicate nanoparticle-tracking experiments, where significant movement of the nanoparticle would appear as a new binding event. Movement could result from the loss of all bonds, reentry into the bulk fluid, and motion downstream with the bulk fluid or a net diffusive motion while remaining bound to the substrate. Detachment profiles were constructed on the basis of the number of nanoparticles that remained bound as a function of time throughout the simulation.

The nanoparticle detachment rate was defined in a similar manner to classical kinetic treatments of molecular binding

$$\frac{dB}{dt} = k_D B \quad (6)$$

where B is the bound particle number. An empirical power law equation was used to capture time-dependent detachment rate behavior, as we previously defined[6]

$$k_D = \frac{k_D^0}{(t/t_{ref})^\beta} \quad (7)$$

where k_D^0 and β are magnitude and temporal parameters, respectively, and t_{ref} is a reference time. t_{ref} simply maintains unit consistency, and we will use a value of 1 s as in previous work. Substituting eq 6 into eq 7 and integrating yields

$$\frac{B}{B_0} = exp\left(k_D^0 \frac{t^{1-\beta}}{\beta - 1}\right) \quad (8)$$

where B_0 is the initial particle number in the ensemble and t is the simulation time.

To ensure statistical significance, we determined detachment parameters for different ensemble numbers and total simulation times. We found that both β and k_D^0 converged for ensemble numbers larger than 150 and simulation times longer than 20 s (Supporting Information, Figure S1). All parameter fits were therefore performed using 200 ensembles and 30 s simulation times. Fitting errors were estimated using the Bootstrap method.

RESULTS

General Dynamics of Nanoparticles and Bonds

As a starting point for an exploration into antibody/ICAM-1 bond mechanical properties, we used 0.1 N/m for both bond spring constants (σ and σ_{ts}), similar to previous BRAD simulations of HIV.[40] We also chose the lowest ICAM-1 coating density (21 μm^{-2}) on the substrate and two different antibody coating densities on the nanoparticle (410 μm^{-2} and 3400 μm^{-2}) from experiments.[6] We then identified γ values that resulted in nanoparticle detachment that varied from stable to unstable regimes. At low antibody density, varying γ from 0.72 to 1.08 nm resulted in continuous nanoparticle detachment throughout the duration of 30 s simulations, with the total number of detached particles ranging from 18% to 99% (Figure 2A). The rate of detachment and total number of detached nanoparticles generally increased with γ. The only exception was a slight crossing over of the detachment curves for γ = 0.78 and 0.82 nm, which we attributed to the stochastic nature of the simulation. Time-varying detachment behavior was clearly evident at high γ, which can be characterized as a rapid decrease during the first 5 s before flattening out beyond 10 s. Mean bond number per bound nanoparticle increased with time (Figure 2B), mirroring the corresponding nanoparticle detachment profile. Surprisingly, final mean bond numbers increased as nanoparticle stability decreased. However, as expected the total number of bonds for the system of 200 nanoparticles decreased with time and correlated with stability (Supporting Information, Figure S2). Similar nanoparticle and bond dynamics were observed at high antibody density, but with higher bound nanoparticle percentages and lower bond numbers for each value of γ (Figures 2C and D). Using eq 8, we fit the detachment curves to obtain the β and k_D^0 parameters. We found that β initially increased with γ before saturating at 0.75 (Figure 2E), which remarkably was the β value we found in experiments. The trend for β was similar for both cases, but shifted to higher γ with increased antibody density. For k_D^0, values correlated with nanoparticle detachment, decreasing with antibody density and increasing steadily with γ (Figure 2F). The latter held true even if β remained

constant at 0.75. The simulation results at γ = 0.92 nm matched experimental findings quite well in terms of both β (~0.75) and k_{D}^{0}. At low antibody density, k_{D}^{0} was nearly identical between simulation and experiment (93 ms^{-1}), but at high density the difference was nearly 5-fold (10 ms^{-1}).

Focusing at the bond level, force played a significant role in destabilizing bonds at high γ. This can be seen in the average bond force at rupture, $F_{\mathrm{B,R}}$, which increased with γ until saturating at around 95 pN (Figure 3A). At the condition best matching experiments (γ = 0.92 nm), average $F_{\mathrm{B,R}}$ was slightly less than 95 pN, with a distribution ranging from 50 to 140 pN (Supporting Information, Figure S3). Average bond force, F_{B}, was significantly lower, however, around 16 pN for the same condition (Supporting Information Figure S3). The mechanical work applied to bonds at rupture, which is the product $\gamma F_{B,R}$, increased steadily with γ (Figure 3B). Interestingly, mechanical work was very close to the bond chemical energy of 87 pN*nm at γ = 0.92 nm, and then continued to increase further at higher γ values. The fact that $F_{\mathrm{B,R}}$ increased as bonds became more sensitive to force (increasing γ) may seem counterintuitive, but this was expected because bond extension (or compression) length at rupture, δ_R, should also increase with γ (Figure 3C). In fact, δ_R remained very close to γ until reaching a maximum at 0.9 nm. It is interesting that $F_{\mathrm{B,R}}$, δ_R, and β all show similar saturation behavior starting at γ = 0.9 nm. As for bond stability, we observed that average lifetime decreased with γ from second to millisecond time-scales (Figure 3D). Though very rare, a few bonds were able to persist the full duration of the simulation (Supporting Information, Figure S3). Bond formation rate increased with γ (Figure 3E), but this was likely a secondary effect driven by decreasing bond stability, as the same bonds could continually break and reform. All bond force and rate metrics shown in Figures 3A–E were identical at high and low antibody density. We did observe that bond formation rate was slightly greater at high antibody density during very early stages of the simulation (s). Final mean bond number at 30 s also varied with antibody density (Figure 3F), ranging between 2.1 and 3.7 bonds per nanoparticle.

Tracking Bond Distributions

To further investigate the inverse correlation between mean bond number and nanoparticle stability (Figure 2B and D, Figure 3F), we constructed histograms of final mean bond number for all conditions (Figures 4A and B). We found that very few particles were bound via a single bond at the end of simulations for any condition and as γ increased, fewer particles remained bound via two or even three bonds. This effect was more pronounced at low antibody density, which can best be seen for the di- and trivalent states. At four bonds and above, adhesion appeared to be insensitive to γ, although sample sizes were small. These findings suggest that γ did not affect the inherent bond distribution attained for a nanoparticle population, only the ability for nanoparticles to successfully remain bound at the lower valencies. Moreover, as the low-valency nanoparticles detached, the bond distribution for the population shifted to a higher mean value. Since this effect is reminiscent of a survival of the fittest scenario, we shall refer to it as valency selection. At high antibody density, the extent of valency selection was diminished for a given value of γ, suppressing the shift in bond number. To account for valency selection, we investigated bond numbers early in the simulation and found that most bonds had already formed within the first 0.1 s

(Supporting Information, Figure S4). This can also be seen by tracking the total bond numbers across the entire system of nanoparticles, which only increased during the first 0.1 s (Supporting Information, Figure S2). Using bond numbers from this early snapshot, when detachment events were minimal, we could eliminate the influence of valency selection and predict the inherent bond distribution available to each nanoparticle population, which were indeed similar regardless of γ (Supporting Information, Figure S5). Corrected mean bond number, or mean bond potential, results are shown in Figure 4C,D as a function of time and confirm that the bond steady state had already been established by the 0.1 s time point. Finally, the mean bond potential did increase with antibody density from approximately 1.7 to 1.9 (Supporting Information, Table S1). Actual mean bond numbers increased over time from these inherent bond potentials exclusively due to valency selection, as the remaining population comprised a steadily increasing number of bonds per nanoparticle.

Mechanical State Diagram

Next we sought to characterize nanoparticle and bond dynamics across a broad range of mechanical parameter space. Therefore, we independently varied σ from 0.001 to 1 N/m and γ from 0.1 to 10 nm and categorized the nanoparticle detachment behavior into one of three states: static, dynamic, or transient. The static and transient states were defined by >95% and <5% of all nanoparticles remaining bound after 5 s, respectively. All other cases were designated as dynamic. Again, using the low antibody density but now paired with medium ICAM-1 density, we constructed the mechanical state diagram shown in Figure 5A. The dynamic regime spanned a continuum of σ and γ combinations but with a stronger sensitivity to γ. We then identified combinations within the dynamic regime that yielded β and k_{D}^{0} values matching experiments, which are listed in Table 2 and depicted as red circles in Figure 5A. For each of these matching cases, bond lifetimes were ~0.1 s and final mean bond numbers were ~3. We did observe differences in $F_{\mathrm{B,R}}$ ranging from 10 to 400 pN, but $\gamma F_{\mathrm{B,R}}$ was consistently close to the bond chemical energy of 87 pN·nm (Table 2). Thus, experimental nanoparticle detachment dynamics, in terms of both temporal behavior and magnitude, could be replicated by matching the bond mechanical work at rupture to the bond chemical energy. We again observed that δ_{R} was close in value to γ under most conditions (Figure 5B), but there appeared to be an inflection point around 50 pN. Because we could not identify a unique γ–σ combination from simulations, we measured the adhesion strength of the antibody/ICAM-1 interaction using optical-tweezers-based force spectroscopy (Supporting Information Methods, Results, and Figure S6). Antibody-coated 3 μm beads were brought into contact with CHO-K1 cells expressing human ICAM-1, and rupture force histograms were obtained at force loading rates of 200, 1500, and 3000 pN/s. The resulting single bond rupture forces were 5.0 ± 2.9, 17.4 ± 4.3, and 52.0 ± 8.9 pN, respectively, which corresponded to γ = 0.27 nm. Using this result, the best-fit σ value was ~0.8 N/m, and this combination is listed in Table 2 and depicted as teal circles in Figure 5.

Final Fitting of Experimental Data

As a final exercise, we simulated all antibody and ICAM-1 density conditions using the γ–σ combination identified in the previous section. β values all ranged between 0.74 and 0.81, very close to 0.75 from experiments (Supporting Information, Table S2). k_{D}^{0} values generally

matched experiments as well (Figure 6A), remaining within a factor of 2 for most conditions. However, no detachment was observed at high ICAM-1 density. Increasing σ had a weak effect at high ICAM-1 but led to significant deviations for the lower ICAM-1 density cases. This led us to postulate that each protein G molecule on the glass substrate may have been able to bind two ICAM dimers. We tested this by modifying our ICAM-1 distribution algorithm to randomly apply protein G molecules at a density equal to one-fourth the high ICAM-1 density (33.5 μm^{-2}). ICAM-1/Fc dimers were then randomly assigned at the appropriate total density. Simulation results under the new clustered ICAM-1 dimer arrangement are listed in Table 3, and k_D^0 values are shown in Figure 6A. The low and medium ICAM-1 densities did not change significantly because most ICAM-1 was still dispersed as single dimers. At high ICAM-1 density though, all ICAM-1 molecules were now clustered in groups of four, which lowered the binding stability such that detachment was now observed under all density conditions. β values were greater than 0.75 from experiments but were also associated with high error because of the small number of detachment events. Fitting k_D^0 with $\beta = 0.75$ resulted in values that were lower than for experiments but within an order of magnitude (Table 3). Because ICAM-1 clustering significantly influenced nanoparticle dynamics, we also performed simulations in which ICAM-1 was distributed entirely as single molecules (Supporting Information, Table S3). Nanoparticle adhesion was most stable for monomers (Figure 6A), with no detachment observed at high ICAM-1 or the medium ICAM-1/high antibody combination. β decreased slightly, ranging from 0.65 to 0.75.

For all conditions simulated, $F_{B,R}$ exceeded 300 pN, increasing modestly with ICAM-1 density and the degree of clustering but remaining insensitive to antibody density (Table 3, see Supporting Information Tables S1 and S2). δ_R exceeded γ by ~50% for most cases, deviating only for the clustered dimer configuration at high ICAM-1 and antibody densities (150%), likely because $F_{B,R}$ was so high at 540 pN (Table 3). Bond lifetimes were all less than 0.2 s, following the same general trend as $F_{B,R}$. Final mean bond numbers ranged from ~2.5 to 7, while again exhibiting evidence of valency selection because very few nanoparticles remained bound via a single bond (Supporting Information, Figure S7). By investigating bond numbers at early time points, we determined that the bond steady state was still attained within 0.1 s for all cases except the clustered dimer configuration at high ICAM-1 density (Supporting Information, Figure S7). For this case, it appeared that there was a second, slower phase of bond accumulation that delayed the steady state to around 0.5 s. After correcting for valency selection, we determined the mean bond potentials for all conditions (Figure 6B). As expected, the mean bond potentials were highest for the monomer configuration, but that for the clustered dimer was slightly greater than that for the dimer even though nanoparticle adhesion was generally less stable. Looking at the bond potential histograms (Figure 6C and Supporting Information, Figure S8), it was clear that the clustered dimer configuration had a broader bond distribution, with more nanoparticles associated with the single bond state. Bond potential histograms also illustrate how bond distributions shifted to higher mean values as the antibody and ICAM-1 density increased. Plotting the mean bond potential versus time confirmed that bonds did not accumulate after the bond steady state was reached within the first 0.1 to 0.5 s of the simulation (Figure 6D

and Supporting Information, Figure S8). Finally, we observed that k_D^0 and the mean bond potential closely followed an exponential relationship across all densities and ICAM-1 configurations (Figure 6E).

DISCUSSION

We have applied the adhesive dynamics simulation framework to investigate how multivalent nanoparticle adhesion to a surface via specific biomolecular interactions stabilizes over time. NAD simulations accurately reproduced the multivalent nanoparticle detachment behavior that we observed in experiments for an antibody/ICAM-1 binding pair. Specifically, the detachment rate (k_D) continually decreased over time following a power law relationship with temporal (β) and magnitude $\left(k_D^0\right)$ fitting parameters (eq 7). The β parameter was insensitive to adhesion molecule densities on the nanoparticle and substrate surfaces, as we observed in experiments. Instead, β was strongly influenced by individual bond stability, with the experimentally observed value ($\beta \approx 0.75$) emerging whenever bonds were subjected to an amount of mechanical work that was equal to the bond chemical energy. The k_D^0 parameter varied with adhesion molecule densities, bond mechanical properties, and ICAM-1 clustering, generally tracking with nanoparticle stability. Although the mean bond number per bound nanoparticle did increase in a manner consistent with the decrease in the nanoparticle detachment rate, we found that this was due to bond accumulation only during the first 0.1–0.5 s of simulations. The mean bond number continued to increase slowly at longer times because nanoparticle populations were heterogeneous with respect to bond potential, and detachment primarily occurred for nanoparticles that were restricted to one or two bonds. This valency selection mechanism resulted in the evolution of the remaining nanoparticle population due to a classic survival of the fittest scenario.

Our results conclusively demonstrated that nanoparticle adhesion was strongly influenced by mechanical forces. Experiments were matched if bonds ruptured under high force ($F_{B,R}$ > 300 pN) or, more accurately, mechanical work ($\gamma F_{B,R} \approx$ bond chemical energy). Bonds were not consistently subjected to this level of force but rather at a frequency such that bonds persisted for ~0.1 s. To put this into context, the half-life for the antibody/ICAM-1 interaction in the absence of force $\left(k_r^0 = 1.1 \times 10^{-4}\,\mathrm{s}^{-1}\right)$ is ~100 min. To further investigate the origin of mechanical force, we conducted a new simulation in which bonds were not allowed to form over time (i.e., $k_f = 0$). Remarkably, all nanoparticles held by a single tether detached in less than 1 s (Figure 7A). Fitting the detachment profile using a simple exponential decay resulted in a rate constant of 3.6 s^{-1}, almost 4 orders of magnitude higher than k_r^0. This finding was not affected by insufficient temporal resolution because the results were identical when we decreased the time step to 0.1 ns (Supporting Information, Figure S9). Bond force (F_B) and rupture force ($F_{B,R}$) distributions for single-tether simulations were similar to the multivalent cases (Figure 7B,C). The average $F_{B,R}$ and bond lifetime were ~290 pN and ~0.25 s, respectively, both very close to the low-valency conditions (Table 3, see Supporting Information, Tables S2 and S3). We found that Brownian motion of the nanoparticle was the only significant source of mechanical force in the single-tether simulation. The shear force was very low at 0.036 pN, and simulation results were not

affected by the removal of fluid flow or increasing the shear rate by a factor of 100 (Supporting Information, Figure S9). Note that the latter finding is consistent with our previous experiments in which nanoparticle detachment rate remained constant after varying the shear rate up to 1000 s^{-1}.[6] As expected, the effects of Brownian motion on detachment correlated with nanoparticle size, further accelerating the detachment rate as the size decreased (Supporting Information, Figure S9). Likewise, increasing size mitigated Brownian effects, particularly because the influence of shear was also rapidly increasing. Shear force became significant only for micrometer-sized particles, but Brownian motion remained the primary source of force inducing bond rupture ($F_{B,R}$ > 200 pN). This is in contrast to a previous study of platelet adhesion, where Brownian motion was determined to have a minimal effect.[41] Although there are differences in the implementation of Brownian motion and fluid shear between these works, adhesive dynamics here versus CDL-BIEM for the platelet case, the key factor is likely the difference in how bonds were modeled. Platelet adhesion was mediated by GPIb-α, which had a much higher γ (0.71 nm) and was not modeled directly as a spring. Regarding the mechanism by which Brownian motion induces bond rupture, Liu et al. previously investigated the adhesion of a 100-nm-diameter sphere mediated by an antibody/mouse ICAM-1 interaction using a thermodynamic model that included an entropic penalty for tethering the nanoparticle's motion.[28] The Bell model was then used to provide an estimate of $F_{B,R}$ that was as high as 230 pN, but no justification was given for the loading rates that were employed. Although this maximum rupture force is similar to the 290 pN value that we found using the single-tether simulation, an important distinction is that our result emerged without having to assume the loading rate.

We have also uncovered a second source of mechanical force, which became more pronounced as bond valency increased and ICAM-1 molecules were clustered (Table 3, see Supporting Information, Tables S2 and S3). We presume that this force arose from bonds pulling on each other. For most cases, interbond pulling was modest, increasing $F_{B,R}$ by only 10–30% relative to the result of the single-tether simulation, but was as high as 100%. We should note that these estimates assume that the contribution of force from nanoparticle Brownian motion remained constant, which may not have been the case. Regardless, it was clear that multivalent nanoparticle adhesion was not stabilized by reducing the mechanical force loads on individual bonds but rather by the fact that the rate of bond formation was simply much faster than rupture for all conditions. Although the mechanically stressed bonds would generally be considered very unstable, persisting only ~0.1 s, we found that the full bond steady state could be attained on this same time scale for nearly all conditions (Figure 6D and Supporting Information, Figure S8). On the basis of the sum of these findings, we conclude that nanoparticles quickly populated and were maintained near their highest valence state, which was likely determined by the local availability of free adhesion molecules. This is supported by the fact that most nanoparticles that detached were able to attain only a maximum of one or two bonds (Figure 7D–F). Specifically, single-bond restricted particles were all lost within ~1 s, similar to the single-bond tether simulation (Figure 7A), but some did persist out to 10 s because of rebinding. For nanoparticles that reached bond valencies of two and even three, detachment tended to occur through the successive loss of all bonds within 0.1 to 0.2 s, thus minimizing the chance for bonds to reform. It should be noted that because only single-bond-restricted nanoparticles were lost at

high ICAM-1 density, it is certainly possible that some nanoparticles detached before reaching their true bond potential.

On the basis of the above findings, we believe that our phenomenological time-dependent detachment rate (eq 7) captures the two critical aspects of valency selection/evolution. Parameter provides a metric for the combined detachment rate of the entire nanoparticle population across the full distribution of bond valencies that are possible, including those nanoparticles that will ultimately detach. The β parameter then modulates this inherent detachment probability as nanoparticles do detach, starting with the initial rapid loss of those restricted to a single bond and then transitioning to the lower multivalent states (Figure 7). To illustrate these concepts, imagine that the nanoparticle population was categorized into i states based on the valency potential, and then each state was assigned a different k_{D}^{0} value (i.e., $k_{\mathrm{D},i}^{0}$) and initial nanoparticle number (i.e., N_{i}). In this scenario, only the N_{i} values would change with time, decaying at a constant rate defined by the respective $k_{\mathrm{D},i}^{0}$, values. The formalization of these valence-state-dependent relationships, including a connection to β, will be a focus of future work. A key implication of this interpretation for time-dependent detachment is that the effects will continue beyond the minute time scale observed in experiments, lasting until only nanoparticles in the highest attainable valence state remain. Our power-law equation is not ultimately bounded in this manner, and thus we cannot extrapolate out to time scales longer than minutes. NAD simulations cannot provide this insight because they are too computationally expensive. Hence, the best approach for predicting long-term behavior will be to develop a deterministic model with rate equations defined for each valence state, similar to previous work.[14–16] Although this requires a large number of parameters to be defined, our simulation results should greatly simplify the process by providing a single-bond rupture rate, the scaling of $F_{\mathrm{B,R}}$ with valency (Table 3), bond potential distributions (Figure 6C), and bonding dynamics during the approach to the steady state (Figure 6D). These insights highlight the advantage of our kinetic approach to understanding multivalent nanoparticle adhesion. Our results also suggest that thermodynamic equilibrium concepts such as affinity or avidity cannot be used to understand multivalent nanoparticle adhesion in a straightforward manner because the population is heterogeneous and will be changing with time. Our work indicates that the ideal time point to define the equilibrium is likely within the first second after binding, but this cannot be assessed experimentally, and even at this time point, the system will have likely already been influenced significantly by valency selection.

Regarding bond biophysics, we found that bonds ruptured after being separated (or compressed) by a length (δ_{R}) very close to γ. This was generally to be expected because γ has mechanistically been described as the length scale for adhesive interactions within the binding pocket.[26] However, δ_{R} is also a length scale related to stretching/compression of the antibody and ICAM-1 molecules, and thus future work will seek to add the necessary molecular detail to distinguish between these different length considerations. Nevertheless, the end result was that over much of the mechanical property parameter space that we investigated, bonds ruptured under mechanical work that was $\sim\sigma\gamma^{2}$. This result is reminiscent of the bond spring energy used in previous adhesive dynamics simulation works,

which was defined as $\sigma\delta^2$.[30,33] However, it is important to clarify that our result was valid only at rupture, with $\gamma\sigma\delta$ prevailing at shorter extension/compression lengths ($\delta < \gamma$). We did attempt to use the $\sigma\delta^2$ relationship in early simulations but could not match the experimental results in terms of β and k_{D}^0. To uniquely identify the bond mechanical properties for our antibody/ICAM-1 pair, we performed force spectroscopy studies using optical tweezers and found γ = 0.27 nm. This is close to the value measured for an antibody/murine ICAM-1 interaction[28] and in general is representative of a moderate bond strength.[26] Extrapolating out to a rupture force of 300 pN would equate to a force loading rate of ~10^8 nN/s, but both of these values are well outside of the range that we used for optical tweezers experiments (maximum ~50 pN). Thus, it is possible that a different energy landscape barrier could be governing bond mechanics, which would equate to a larger γ.[26] This force regime will be examined experimentally in future studies. Using γ = 0.27 nm, we found that σ = 0.8 N/m provided the best fit to experiments, placing δ_{R} at ~0.4 nm, or approximately 50% larger than γ. Our σ value was larger than in previous works using HIV or nanoparticles[28,38–40] but was not so high as to introduce artifacts into the simulation. This was determined on the basis of the spring time $\tau_\sigma = 2\pi\sqrt{m/\sigma}$, where m is the mass of the particle.[48] The value of τ_σ was ~16 ns, which is an order of magnitude greater than the time step used for simulations and 5-fold greater than the viscous relaxation time (2 ns, see Supporting Information).

Using our final mechanical parameters, we achieved excellent correlation between NAD simulations and experiments in terms of both β and k_{D}^0 kinetic parameters at most, but not all, adhesion molecule densities. Because no detachment was observed at high ICAM-1 density, we chose to cluster ICAM-1 dimers in a manner that was consistent with our experimental setup using protein G molecules to bind ICAM-1/Fc. This change successfully destabilized the results at high ICAM-1 without negatively affecting the other cases. If we consider the valence-state concepts introduced in the preceding paragraphs, then fine-tuning σ primarily modulated the inherent detachment rates for each valence state (i.e., $k_{\mathrm{D},i}^0$ values), while clustering ICAM-1 primarily redistributed the initial number of nanoparticles in each valence state (i.e., N_{i} values, see Figure 6C and Supporting Information, Figure S8, for examples). Even though the final kinetic consistency between NAD simulations and experiments was very strong, deviations still remained. It is possible that the fitting could be improved by further adjusting σ or the molecular configurations (i.e., clustering, discrete physical detail). Alternatively, simulations may overestimate the bond-formation rate, which could be adjusted by decoupling σ_{ts} from σ or by tracking the orientation of unbound adhesion molecules to account for the actual separation distance between binding domains. Another related phenomenon is that we did not prevent bonds from occupying the same physical space as nanoparticles translated and rotated, which would be expected to have a larger effect at higher bond valencies. We did prevent new bonds from forming if they were within 2 nm of another bond, but this estimate may have been too conservative. Finally, discrepancies may simply be related to measurement errors within the experiments.

In future work, we will expand our NAD simulations to include tethering from the bulk fluid to model the nanoparticle attachment rate (k_{A}), enabling full kinetic evaluation of the

experimental binding data. We will also incorporate discrete physical details for receptor and ligand molecules to increase accuracy and better represent bond biophysics. It will also be extremely valuable to explore a broader range of parameter space across experiments and simulations, including nanoparticle size and shape as well as bond kinetics and mechanics, and we have already tested some of these parameters in previous experiments.[8,11] Regarding potential targeted delivery applications, we will begin to evaluate adhesive behavior in a cellular context. This will require that target ligands be allowed to diffuse laterally within the plasma membrane and potentially be translated in response to force. The motion of the ligand within the substrate would follow similar treatments used here for nanoparticles, as demonstrated in previous work.[39,40] Finally, we will develop deterministic rate models to capture valence-state-dependent dynamics, further investigate the fundamental basis of the k_{D}^{0} and β parameters, predict the long-term behavior of nanoparticle populations, and provide bond-scale analysis in a more computationally accessible manner than do NAD simulations. On the basis of our combined experimental and computational approaches, we anticipate that new and powerful strategies will be uncovered that will enable greater control over nanoparticle adhesion and maximize targeting performance. Our unique kinetic approach may even make it possible to direct early-stage behavior toward different final states.

Supplementary Material

Refer to Web version on PubMed Central for supplementary material.

Acknowledgments

We thank Dr. Jun Allard for helpful conversations and review of the article. We also thank Ting-Yi Chu for assistance with experiments. This work was supported in part by the National Science Foundation under award number 1539114, the National Institutes of Health under award P41-RR001192 “A Laser Microbeam Biotechnology Resource (LAAMP)”, and a gift from AutoDesk, Inc. Any opinions, findings, and conclusions or recommendations expressed in this material are those of the authors and do not necessarily reflect the views of the National Science Foundation.

References

1. Peer D, Karp JM, Hong S, Farokhzad OC, Margalit R, Langer R. Nanocarriers as an emerging platform for cancer therapy. Nat Nanotechnol. 2007; 2:751–760. [PubMed: 18654426]
2. Davis ME, Chen ZG, Shin DM. Nanoparticle therapeutics: an emerging treatment modality for cancer. Nat Rev Drug Discovery. 2008; 7:771–782. [PubMed: 18758474]
3. Cheng Z, Al Zaki A, Hui JZ, Muzykantov VR, Tsourkas A. Multifunctional nanoparticles: cost versus benefit of adding targeting and imaging capabilities. Science. 2012; 338:903–910. [PubMed: 23161990]
4. Muro S, Dziubla T, Qiu W, Leferovich J, Cui X, Berk E, Muzykantov VR. Endothelial targeting of high-affinity multivalent polymer nanocarriers directed to intercellular adhesion molecule 1. J Pharmacol Exp Ther. 2006; 317:1161–1169. [PubMed: 16505161]
5. Hong S, Leroueil PR, Majoros IJ, Orr BG, Baker JRJ, Banaszak Holl MM. The binding avidity of a nanoparticle-based multivalent targeted drug delivery platform. Chem Biol. 2007; 14:107–115. [PubMed: 17254956]
6. Haun JB, Hammer DA. Quantifying nanoparticle adhesion mediated by specific molecular interactions. Langmuir. 2008; 24:8821–8832. [PubMed: 18630976]
7. Jiang W, Kim BY, Rutka JT, Chan WC. Nanoparticle-mediated cellular response is size-dependent. Nat Nanotechnol. 2008; 3:145–150. [PubMed: 18654486]

8. Haun JB, Robbins GP, Hammer DA. Engineering therapeutic nanocarriers with optimal adhesion for targeting. J Adhes. 2010; 86:131–159.
9. Tassa C, Duffner JL, Lewis TA, Weissleder R, Schreiber SL, Koehler AN, Shaw SY. Binding affinity and kinetic analysis of targeted small molecule-modified nanoparticles. Bioconjugate Chem. 2010; 21:14–19.
10. Wang J, Tian S, Petros RA, Napier ME, Desimone JM. The complex role of multivalency in nanoparticles targeting the transferrin receptor for cancer therapies. J Am Chem Soc. 2010; 132:11306–11313. [PubMed: 20698697]
11. Haun JB, Pepper LR, Boder ET, Hammer DA. Using engineered single-chain antibodies to correlate molecular binding properties and nanoparticle adhesion dynamics. Langmuir. 2011; 27:13701–13712. [PubMed: 21942413]
12. Zern BJ, Chacko AM, Liu J, Greineder CF, Blankemeyer ER, Radhakrishnan R, Muzykantov V. Reduction of nanoparticle avidity enhances the selectivity of vascular targeting and PET detection of pulmonary inflammation. ACS Nano. 2013; 7:2461–2469. [PubMed: 23383962]
13. Wiley DT, Webster P, Gale A, Davis ME. Transcytosis and brain uptake of transferrin-containing nanoparticles by tuning avidity to transferrin receptor. Proc Natl Acad Sci U S A. 2013; 110:8662–8667. [PubMed: 23650374]
14. Kitov PI, Bundle DR. On the nature of the multivalency effect: a thermodynamic model. J Am Chem Soc. 2003; 125:16271–16284. [PubMed: 14692768]
15. Huskens J, Mulder A, Auletta T, Nijhuis CA, Ludden MJ, Reinhoudt DN. A model for describing the thermodynamics of multivalent host-guest interactions at interfaces. J Am Chem Soc. 2004; 126:6784–6797. [PubMed: 15161307]
16. Diestler DJ, Knapp EW. Statistical thermodynamics of the stability of multivalent ligand-receptor complexes. Phys Rev Lett. 2008; 100:178101. [PubMed: 18518340]
17. Wang S, Dormidontova EE. Nanoparticle design optimization for enhanced targeting: Monte Carlo simulations. Biomacromolecules. 2010; 11:1785–1795. [PubMed: 20536119]
18. Wang S, Dormidontova EE. Nanoparticle targeting using multivalent ligands: computer modeling. Soft Matter. 2011; 7:4435–4445.
19. Wang S, Dormidontova EE. Selectivity of ligand-receptor interactions between nanoparticle and cell surfaces. Phys Rev Lett. 2012; 109:238102. [PubMed: 23368269]
20. Martinez-Veracoechea FJ, Frenkel D. Designing super selectivity in multivalent nano-particle binding. Proc Natl Acad Sci U S A. 2011; 108:10963–10968. [PubMed: 21690358]
21. Bell GI. Models for the specific adhesion of cells to cells. Science. 1978; 200:618–627. [PubMed: 347575]
22. Florin EL, Moy VT, Gaub HE. Adhesion forces between individual ligand-receptor pairs. Science. 1994; 264:415–417. [PubMed: 8153628]
23. Alon R, Hammer DA, Springer TA. Lifetime of the P-selectin-carbohydrate bond and its response to tensile force in hydrodynamic flow. Nature. 1995; 374:539–542. [PubMed: 7535385]
24. Evans E, Ritchie K, Merkel R. Sensitive force technique to probe molecular adhesion and structural linkages at biological interfaces. Biophys J. 1995; 68:2580–2587. [PubMed: 7647261]
25. Evans E, Ritchie K. Dynamic strength of molecular adhesion bonds. Biophys J. 1997; 72:1541–1555. [PubMed: 9083660]
26. Merkel R, Nassoy P, Leung A, Ritchie K, Evans E. Energy landscapes of receptor-ligand bonds explored with dynamic force spectroscopy. Nature. 1999; 397:50–53. [PubMed: 9892352]
27. Decuzzi P, Ferrari M. Design maps for nanoparticles targeting the diseased microvasculature. Biomaterials. 2008; 29:377–384. [PubMed: 17936897]
28. Liu J, Weller GE, Zern B, Ayyaswamy PS, Eckmann DM, Muzykantov VR, Radhakrishnan R. Computational model for nanocarrier binding to endothelium validated using in vivo, in vitro, and atomic force microscopy experiments. Proc Natl Acad Sci U S A. 2010; 107:16530–16535. [PubMed: 20823256]
29. Djohari H, Dormidontova EE. Kinetics of nanoparticle targeting by dissipative particle dynamics simulations. Biomacromolecules. 2009; 10:3089–3097. [PubMed: 19894765]

30. Hammer DA, Apte SM. Simulation of cell rolling and adhesion on surfaces in shear flow: general results and analysis of selectin-mediated neutrophil adhesion. Biophys J. 1992; 63:35–57. [PubMed: 1384734]
31. Chang KC, Tees DF, Hammer DA. The state diagram for cell adhesion under flow: leukocyte rolling and firm adhesion. Proc Natl Acad Sci U S A. 2000; 97:11262–11267. [PubMed: 11005837]
32. Chang KC, Hammer DA. Adhesive dynamics simulations of sialyl-Lewis(x)/E-selectin-mediated rolling in a cell-free system. Biophys J. 2000; 79:1891–1902. [PubMed: 11023895]
33. King MR, Hammer DA. Multiparticle adhesive dynamics. Interactions between stably rolling cells. Biophys J. 2001; 81:799–813. [PubMed: 11463626]
34. King MR, Hammer DA. Multiparticle adhesive dynamics: hydrodynamic recruitment of rolling leukocytes. Proc Natl Acad Sci U S A. 2001; 98:14919–14924. [PubMed: 11752440]
35. Beste MT, Hammer DA. Selectin catch-slip kinetics encode shear threshold adhesive behavior of rolling leukocytes. Proc Natl Acad Sci U S A. 2008; 105:20716–20721. [PubMed: 19095798]
36. Mody NA, King MR. Platelet adhesive dynamics. Part I: characterization of platelet hydrodynamic collisions and wall effects. Biophys J. 2008; 95:2539–2555. [PubMed: 18515387]
37. Mody NA, King MR. Platelet adhesive dynamics. Part II: high shear-induced transient aggregation via GPIbalpha-vWF-GPIbalpha bridging. Biophys J. 2008; 95:2556–2574. [PubMed: 18515386]
38. English TJ, Hammer DA. Brownian adhesive dynamics (BRAD) for simulating the receptor-mediated binding of viruses. Biophys J. 2004; 86:3359–3372. [PubMed: 15189840]
39. English TJ, Hammer DA. The effect of cellular receptor diffusion on receptor-mediated viral binding using Brownian adhesive dynamics (BRAD) simulations. Biophys J. 2005; 88:1666–1675. [PubMed: 15556985]
40. Trister AD, Hammer DA. Role of gp120 trimerization on HIV binding elucidated with Brownian adhesive dynamics. Biophys J. 2008; 95:40–53. [PubMed: 18339756]
41. Mody NA, King MR. Influence of Brownian motion on blood platelet flow behavior and adhesive dynamics near a planar wall. Langmuir. 2007; 23:6321–6328. [PubMed: 17417890]
42. Allen, MP., Tildesley, DJ. Computer Simulation of Liquids. Clarendon Press; 1989.
43. Chandrasekhar S. Stochastic problems in physics and astronomy. Rev Mod Phys. 1943; 15:1–89.
44. Bell GI, Dembo M, Bongrand P. Cell adhesion. Competition between nonspecific repulsion and specific bonding. Biophys J. 1984; 45:1051–1064. [PubMed: 6743742]
45. Goldman AJ, Cox RG, Brenner H. Slow viscous motion of a sphere parallel to a plane wall—II Couette flow. Chem Eng Sci. 1967; 22:653–660.
46. Qian J, Wang J, Gao H. Lifetime and strength of adhesive molecular bond clusters between elastic media. Langmuir. 2008; 24:1262–1270. [PubMed: 18179265]
47. Eniola AO, Willcox PJ, Hammer DA. Interplay between rolling and firm adhesion elucidated with a cell-free system engineered with two distinct receptor-ligand pairs. Biophys J. 2003; 85:2720–2731. [PubMed: 14507735]
48. Yu HY, Eckmann DM, Ayyaswamy PS, Radhakrishnan R. Composite generalized Langevin equation for Brownian motion in different hydrodynamic and adhesion regimes. Phys Rev E. 2015; 91:052303.

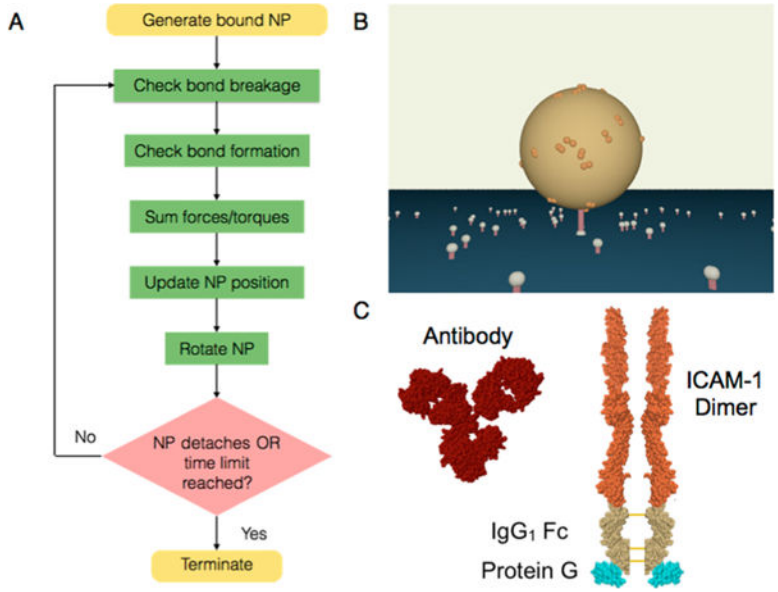

Figure 1.

NAD simulations of nanoparticle detachment. (A) Algorithm for detachment simulations in which nanoparticles were initiated with a single bond. (B) Schematic of the adhesion system. A 210-nm-diameter sphere was coated with monoclonal anti-ICAM-1 antibody (orange), and the substrate was coated with ICAM-1 dimers (gray). (C) Size-scaled depiction of the adhesion molecule system employed. Images are published in the Protein Data Bank: mouse IgG_1 antibody (1IGY), ICAM-1 (combination of 1IAM and 1P53), human IgG_1 Fc (3D03), and protein G (3GB1).

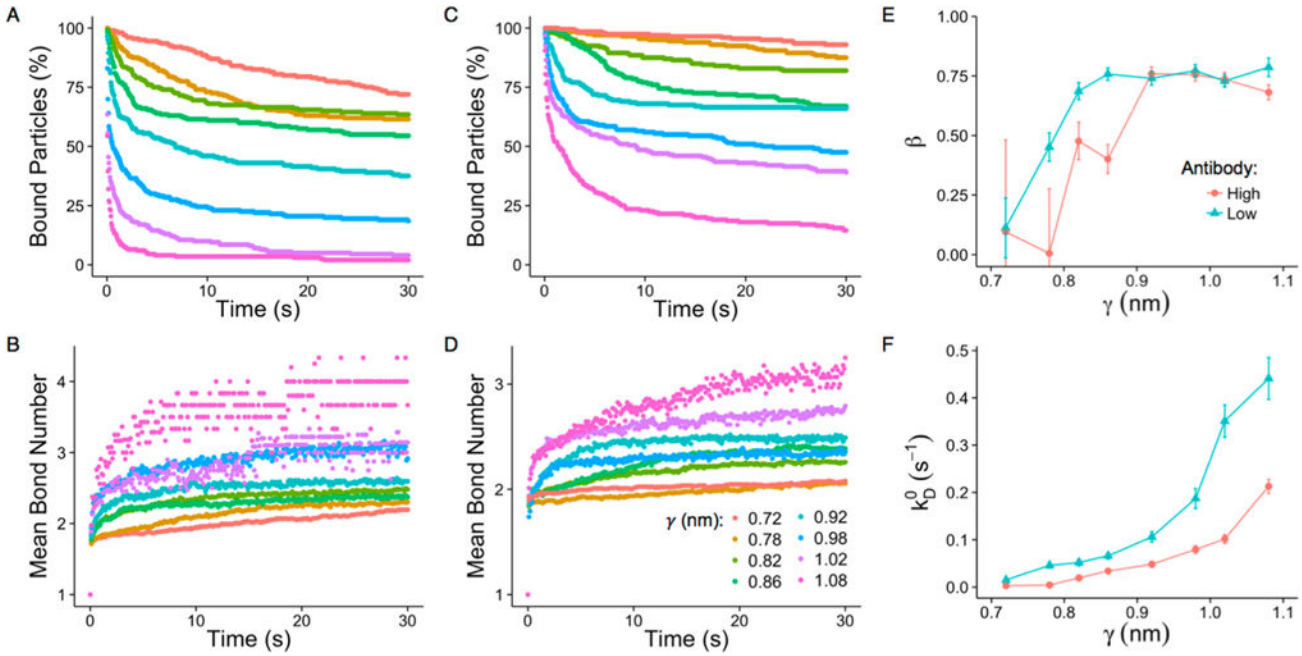

Figure 2.

Nanoparticle and bond dynamics. (A,C) Nanoparticle detachment profiles obtained for σ = 0.1 N/m, γ = 0.72 to 1.08 nm, and low ICAM-1 density at (A) low and (C) high antibody density. Time-dependent behavior can clearly be seen at high γ, with an initial rapid decline that transitioned to a more stable regime around ~5 s. (B,D) Mean bond number increased over time for both (B) low and (D) high antibody density conditions following a similar temporal pattern as nanoparticle detachment. Bond number increased and became more stochastic as fewer nanoparticles remained bound. (E,F) Detachment profiles were fit using eq 7 to obtain (E) β and (F) k_{D}^{0} parameters. (E) The temporal parameter β increased with γ until saturating at 0.75, which was the value measured in experiments. There was a slight shift to higher γ as antibody density increased. (F) The magnitude parameter k_{D}^{0} progressively increased with γ and decreased with antibody density regardless of β, reflecting overall nanoparticle stability.

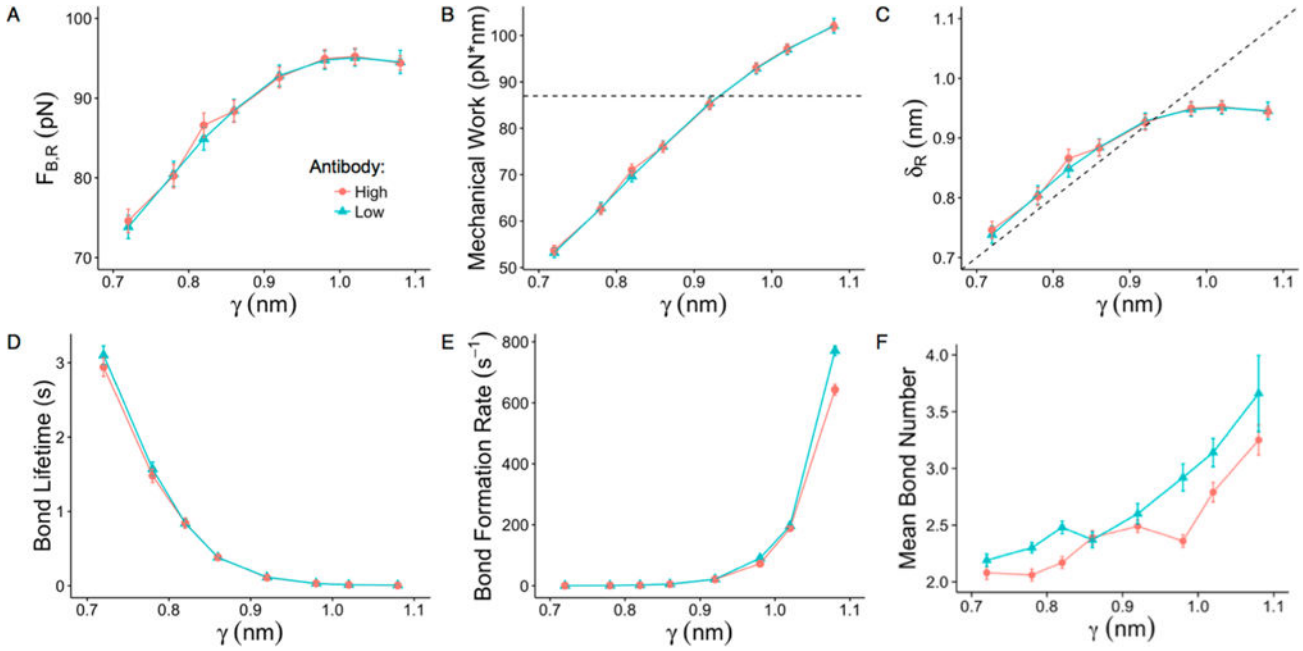

Figure 3.

Bond biophysics and dynamics. (A) Bond rupture force ($F_{B,R}$) increased with γ before saturating around 95 pN. (B) Mechanical work at bond rupture ($\gamma F_{B,R}$) increased steadily with γ, surpassing the bond chemical energy (dashed line) around 0.9 nm. (C) Bond extension or compression length at rupture (δ_R) was slightly greater than γ until saturating around 0.9 nm. (D,E) Average bond (D) lifetime and (E) formation rate exhibited opposing trends as bonding became more dynamic with increased γ. (F) Mean bond number at the end of simulation (30 s) increased as adhesion became less stable, both in terms of increasing γ and decreasing antibody density. Error bars represent the standard error from 200 simulations.

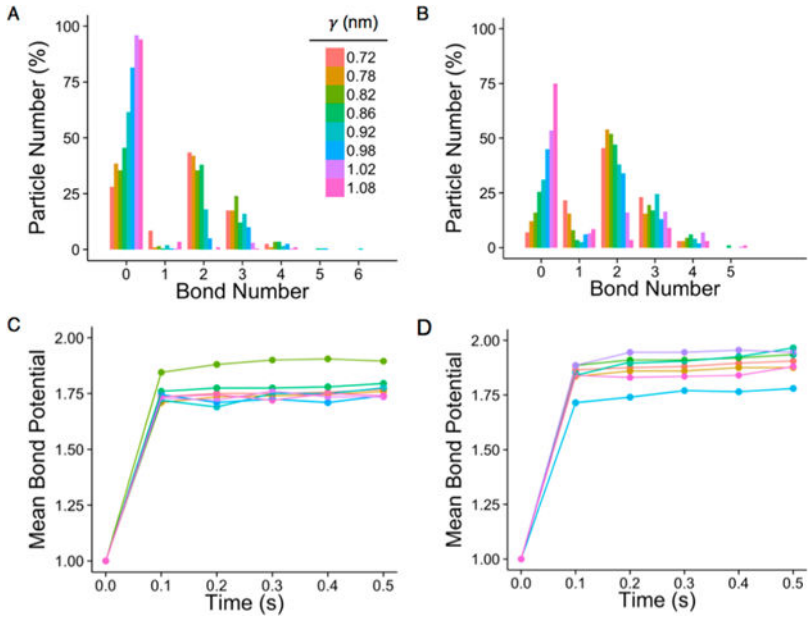

Figure 4.

Bond number distributions and potentials. (A, B) Bond number histograms obtained at the end of simulations (30 s) for $\sigma = 0.1$ N/m, $\gamma = 0.72$ to 1.08 nm, and a low ICAM-1 density at (A) low and (B) high antibody densities. Detached nanoparticles were categorized under 0 bonds. (C, D) Mean bond potential values as a function of time at (C) low and (D) high antibody densities. The mean bond potential represents the mean bond number determined right after the bond steady state was achieved (0.1 s) and after correcting for nanoparticles that had detached. The mean bond potential did not vary with γ but shifted from ~1.7 to ~1.9 with increased antibody density.

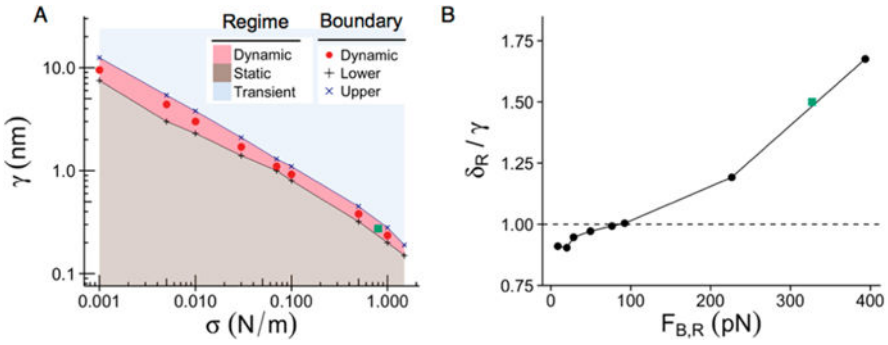

Figure 5.

Mechanical state diagram. (A) Nanoparticle detachment dynamics at low antibody and medium ICAM-1 densities, assessed across a large range of γ and σ values. The transient regime (blue) corresponds to highly unstable adhesion, defined as <5% of nanoparticles remaining bound after 5 s. The static regime (brown) corresponds to highly stable adhesion, with >95% remaining bound after 5 s. The dynamic regime (red) lies in between, and the red circles indicate the mechanical property combinations that precisely matched experiments. (B) The bond rupture length (δ_R) was slightly less than γ at low $F_{B,R}$ but became increasingly larger after $F_{B,R}$ exceeded ~95 pN. Teal squares denote the matching condition using γ measured with optical tweezers force spectroscopy experiments (0.27 nm) and the best fit σ (0.8 N/m).

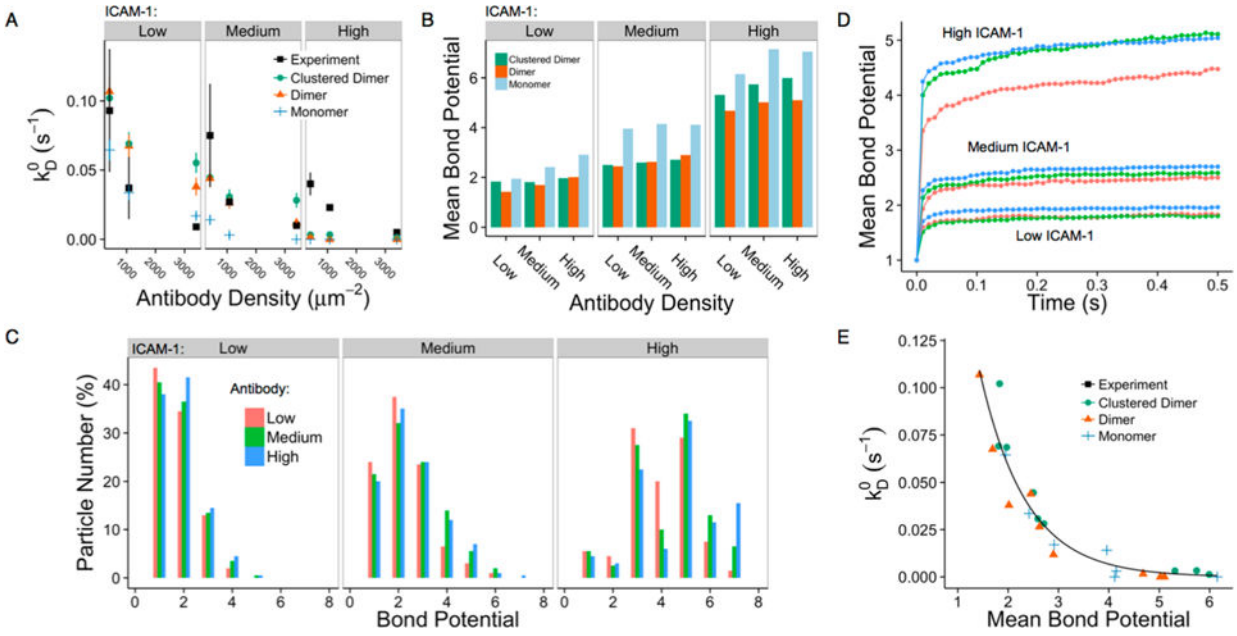

Figure 6.

Final fitting of experiments for different ICAM-1 clustering conditions. (A) Comparison of k_{D}^{0} across all antibody and ICAM-1 densities between experiments and NAD simulations conducted using the final mechanical conditions (γ = 0.27 nm, σ = 0.8 N/m). ICAM-1 was presented in three different configurations: dimers, clustered dimers, and monomers. The clustering of ICAM-1 decreased the nanoparticle stability, particularly at high ICAM-1 density. (B) The mean bond potential was highest for ICAM-1 monomers. Dimer configurations were similar at low and medium ICAM-1, but the clustered dimer surprisingly had elevated mean bond potentials at high ICAM-1. (C) Bond potential histograms for the clustered dimer case. Note the large number of nanoparticles restricted to one or two bonds at low and medium ICAM-1 densities. (D) Mean bond potential versus time for the clustered dimer case, shown only at early time points to illustrate that the bond steady state was reached before 0.1 s at low and medium ICAM-1 densities. At high ICAM-1 density, most bonds formed prior to 0.1 s, but a second, slower bond accumulation phase was also observed out to 0.5 s. (E) k_{D}^{0} and mean bond potential closely followed an exponential relationship for all molecular density and ICAM-1 clustering conditions.

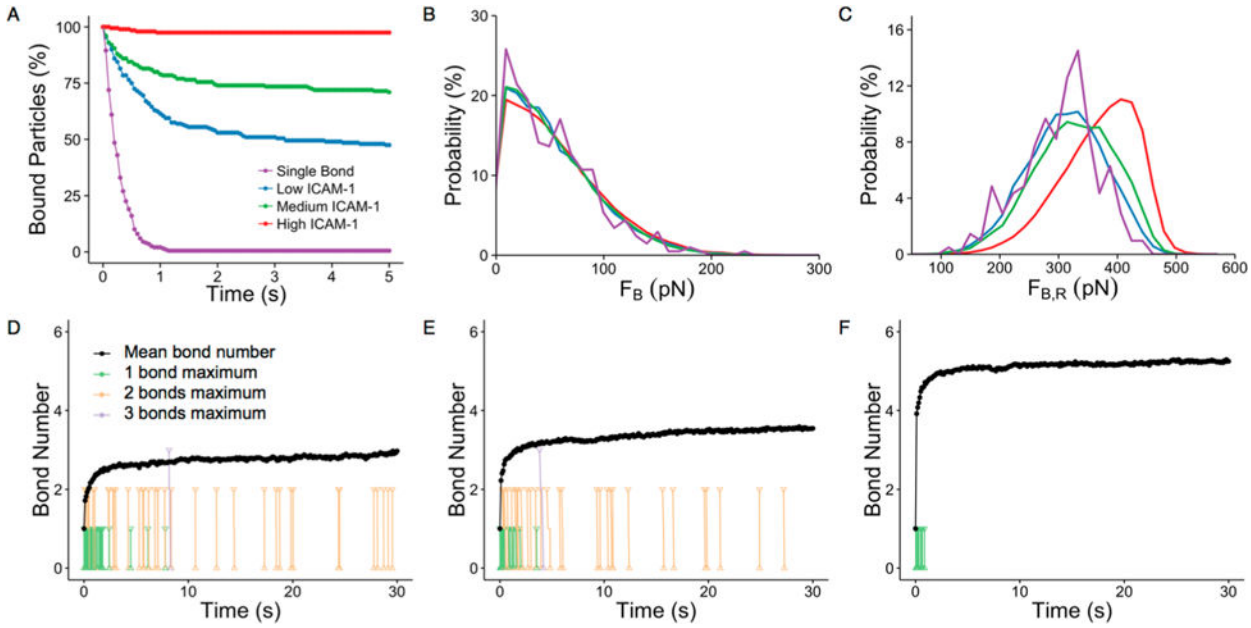

Figure 7.

Single-tether simulations and valence-state-dependent detachment dynamics. (A) Nanoparticles held by a single tether all detached within 1 s, with a profile that closely resembled the initial phase of rapid detachment observed for multivalent cases. (B) The bond force distribution for the single-tether simulation was nearly identical to the multivalent cases. (C) Bond rupture force distributions were similar between the single tether and low ICAM-1 density cases, but the rupture force shifted to higher values with increased valency. (D–F) Valence-state-dependent detachment dynamics. The mean bond number (black line) is shown over time at low antibody density and either (D) low, (E) medium, or (F) high ICAM-1 density. All detachment events are included in the plot and color-coded on the basis of the maximum bond number achieved: one bond (green), two bonds (orange), or three bonds (purple). The point of detachment is indicated by the triangle (△), and lines then trace back up to the time point at which that nanoparticle was at its maximum bond number, which is indicated by an upside down triangle (▽). Nanoparticles restricted to a single bond detached rapidly, most within the first few seconds. Nanoparticles that detached from the second and third bond states persisted longer and quickly dropped all the way to zero bonds, typically within 0.1 s, limiting the chance for bonds to reform.

Table 1

Physical Parameters Used in NAD Simulations

parameter	parameter	value	dimension
R	nanoparticle radius	105	nm
ρ	nanoparticle density	1.05	g/cm^3
λ_e	equilibrium bond length	41.1	nm
	antibody length	11.4	nm
	ICAM-1 length	29.7	nm
	antibody density	410/1080/3400	μm^{-2}
	ICAM-1 density	21/41/134	μm^{-2}
k_f^0	intrinsic bond formation rate	1.6×10^5	s^{-1}
k_r^0	intrinsic bond breakage rate	1.1×10^{-4}	s^{-1}
μ	viscosity	0.001	g/nm·s
T	temperature	300	K
Δt	time step	1	ns
S	fluid shear rate	100	s^{-1}
τ	polymer thickness	5	nm
ξ	compressibility	0.03	pN

Table 2

Different γ and σ Combinations Resulting in Nanoparticle Dynamics That Match Experimental Results

σ (N/m)	γ (nm)	β	k_D^0 (ms^{-1} D)	$F_{B,R}$ (pN)	δ_R (nm)	rupture work (pN·nm)
0.001	9.5	0.77 ± 0.02	140 ± 10	8.6	8.6	81.7
0.005	4.4	0.75 ± 0.03	140 ± 10	19.9	4.0	87.6
0.01	3	0.81 ± 0.02	90 ± 10	28.4	2.8	85.2
0.03	1.7	0.78 ± 0.03	90 ± 10	49.5	1.7	84.2
0.07	1.1	0.75 ± 0.03	100 ± 10	76.4	1.1	84.0
0.1	0.92	0.79 ± 0.02	110 ± 10	92.3	0.9	84.9
0.5	0.38	0.74 ± 0.03	150 ± 10	226.4	0.5	86.0
0.8	0.27	0.78 ± 0.04	47 ± 6	324.4	0.4	87.6
1	0.24	0.75 ± 0.02	120 ± 10	393.7	0.4	94.5

Table 3

Final Simulation Results across All Valency Conditions for $\gamma = 0.27$ nm, $\sigma = 0.8$ N/m, and the Clustered Dimer Configuration for ICAM-1

ICAM-1 (μm^2)	Ab (μm^{-2})	β	k_D^0 (ms^{-1})	bound NP (%)	bond lifetime (s)	$F_{B,R}$ (pN)	rupture work (pN·nm)	δ_R (nm)	final bond number	bond potential
21	410	0.80 ± 0.02	102 ± 10	39	0.15	311.7	85.4	0.39	2.8	1.8
21	1080	0.77 ± 0.03	69 ± 8	54	0.15	314.8	86.3	0.39	2.8	1.8
21	3400	0.68 ± 0.03	55 ± 7	56	0.16	312.9	85.7	0.39	2.5	2.0
41	410	0.82 ± 0.03	52 ± 6	64	0.10	327.0	89.6	0.41	3.5	2.5
41	1080	0.83 ± 0.02	31 ± 5	73	0.11	328.2	89.9	0.41	3.3	2.6
41	3400	0.75 ± 0.03	28 ± 5	79	0.10	329.6	90.3	0.41	3.3	2.7
134	410	0.94 ± 0.68	3 ± 1[a]	98	0.03	369.1	101.1	0.46	5.5	5.3
134	1080	0.93 ± 0.55	3 ± 2[a]	97	0.02	373.5	102.3	0.47	5.9	5.7
134	3400	0.99 ± 0.44	1 ± 1[a]	99	0.02	542.1	148.5	0.68	6.1	6.0

[a] Fitting of k_D^0 was performed using $\beta = 0.75$.